Development of a Control-Oriented Model of Floating Wind Turbines

Giulio Betti, Marcello Farina, Giuseppe A. Guagliardi, Andrea Marzorati, and Riccardo Scattolini

I. INTRODUCTION

IN 2010, the world witnessed an increase of over 24% of wind power capacity with respect to the total power produced in 2009. In particular, in the European Union (EU), the wind power represented the 10% of the total power generation capacity and the 5.3% of gross EU power consumption. This has huge positive environmental effects, with a reduction of about 115 tons of the CO_2 annual emissions [2].

In this context, researchers are putting much effort in the development of deep water offshore wind turbines, which can operate in large areas characterized by strong and consistent winds, without logistic limitations in the size of the turbines or problems due to their visual and noise annoyances [3], [4]. In deep water, floating support platforms are one of the most promising solutions, from an economic and technical standpoint [5]; however, the definition of the most effective floating configuration structures is still a largely open issue. Different floating configurations have been proposed, e.g., spar-buoy platform (SP), tension leg platform (TLP) and Barge Platform (BP) [3], [4], [6]–[10].

Detailed mathematical models of floating turbines, including hydrodynamic, platform, and mooring dynamics, have been developed [4], [6], [11]–[15] as tools for the analysis of the system dynamics, turbine loads, fatigue damage, and cost assessment. In [14], a model of a turbine mounted on a SP and of a multiple-unit floating offshore wind farm has been developed. In [4] and [6], TLPs have been analyzed using a detailed simulator named BM. In [16], available simulation software packages for offshore wind turbines (namely HAWC2, OnWind and Bladed) have been compared. A recent review of available floating wind turbines design tools can be found in [17].

In [11]–[13], a comprehensive dynamic model has been developed and used for the analysis of the three floating configurations listed above. The corresponding simulation environment, named FAST, has been used in [1] to compare the characteristics of SP, TLP, and BP platforms, drawing the conclusion that some advantages can be highlighted for TLP and SP in terms of reduction of loads on the turbine components. In view of its accuracy, flexibility, generality, and free availability, nowadays FAST has become one of the most used simulation tools, both for on-land and for off-shore wind turbines.

Despite the availability of reliable software environments, based on very detailed and complex mathematical descriptions, it is still of interest to develop simpler, yet accurate physical models, able to represent the main dynamics of the overall structure and specifically suited for the controller synthesis. In fact, these models can be useful to: 1) provide a clear and immediate understanding of the main physical phenomena involved; 2) easily modify the model to describe different and/or novel configurations and apparatuses; 3) design linear and nonlinear control laws with well established techniques, which could not be carried out with available very large-scale models; and 4) quickly test in a preliminary phase different control configurations and/or tunings, to be subsequently validated and refined with detailed linear and/or nonlinear models. For these reasons, in the first part of this paper, a low order physical model of a TLP floating turbine is presented and validated with respect to the accurate FAST simulator. This model is then used to design a multivariable realistic controller with H_∞ control [18], [19]. The H_∞ synthesis approach has been chosen in view of its robustness properties, which become more and more important when simplified models are used for design, as in the case here considered. Concerning the control of variable-speed wind turbines, it is worth recalling that they operate in three main regimes, depending on the wind speed v_{in} (see Fig. 1): in Region R1 (where either $v_{\text{in}} < v_{\text{cut-in}}$ or $v_{\text{in}} \geq v_{\text{cut-out}}$), the turbine is switched off for safety reasons; in Region R2 (where $v_{\text{cut-in}} \leq v_{\text{in}} < v_{\text{rated}}$), the objective is the

Manuscript received January 31, 2012; revised December 13, 2012; accepted January 13, 2013. Manuscript received in final form January 18, 2013. Date of publication February 6, 2013; date of current version December 17, 2013. This work was supported by RSE SpA. Recommended by Associate Editor J. Y. Lew.

G. Betti, M. Farina, A. Marzorati, and R. Scattolini are with the Dipartimento di Elettronica e Informazione, Politecnico di Milano, Milano 20133, Italy (e-mail: betti@elet.polimi.it; farina@elet.polimi.it; andrea.87@hotmail.it; riccardo.scattolini@elet.polimi.it).

G. A. Guagliardi is with R.S.E. SpA, Milano 20100, Italy (e-mail: Giuseppe.Guagliardi@rse-web.it).

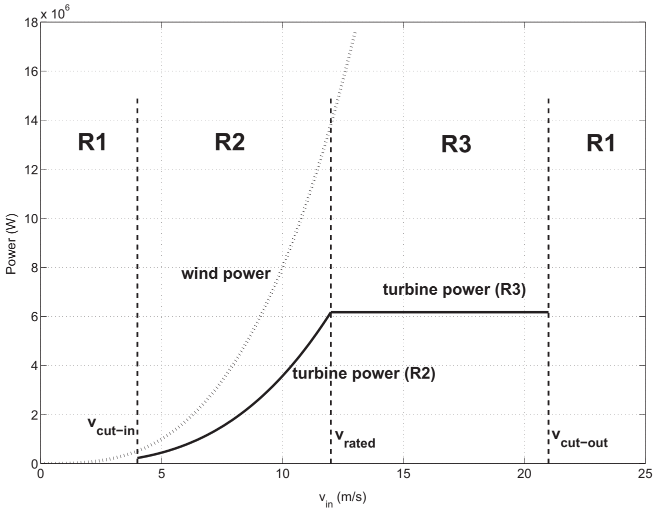

Fig. 1. Wind power versus produced electrical power in the three operational regimes.

maximization of the produced energy; in Region R3 (where $v_{\text{rated}} \leq v_{\text{in}} < v_{\text{cut-out}}$), the captured wind energy is limited in order to avoid dangerous electrical and mechanical loads.

Examples of standard and advanced control techniques for onshore variable speed wind turbines can be found in [20]–[28]; an exhaustive description is also presented in [24] and [29], where the authors propose a multi-input strategy with the aim to fulfill the multiple objective of regulating the rotor speed and the produced power, and to avoid significant loads. The joint use of blade pitch and torque is also proposed in [20] to improve the trade-off between energy and loads. Light detector and ranging (LIDAR) assisted control strategies have recently been proposed [30].

Less attention has been paid so far to the control of offshore floating wind turbines [8]–[10], [31], although in this case the control problem is more difficult and relevant, due to the need to limit the extra motions of the system.

In particular, the above rated wind speed Region R3 reveals critical control aspects; negative damping of platform pitch can easily arise, due to the fact that the wind thrust decreases when the wind speed increases [8] and [32]. In [10], a control algorithm has been developed to avoid the stability problems that could occur with traditional pitch control. In [9], a detailed analysis of the pitch damping of a floating turbine controlled with different methods is presented. In [8] and [31], a multi-input optimal control strategy is proposed in Region R3.

In this paper, an H_∞ approach is used for the design of a regulator for control of the rotor speed and of the pitch oscillations in Region R3. The H_∞ control approach has been already used, in view of its well-known robustness properties, for control of on-shore wind turbines, as discussed in [33]–[35]. In this paper, this technique has been selected also because it makes it possible to address the problem of attenuating disturbances acting on the floating system characterized by known frequency spectra, namely, wind fluctuations and waves, see Section II-C. In order to test the regulator performances, wind and waves have also been simulated according to the results of [36]–[38]. The proposed H_∞ regulator has been validated in simulation both on the simplified dynamic model used for its development and on the FAST reference simulator.

This paper is organized as follows. Section II presents the simplified mathematical models of the wind turbine, of the TLP structure, and of wind and waves. The results of the model identification and validation with respect to the reference model FAST are shown in Section III. In Section IV, a brief description of the proposed control strategy is given and the simulation results of the proposed controller are compared to those obtained with the PI-based control structure available in the FAST simulator. In Section V, some conclusions are drawn.

For clarity of presentation, the detailed equations of the TLP model as well as the numerical values of its parameters are given in Appendixes I and II.

II. MODEL OF THE SYSTEM

In this section, the models of the wind turbine and of the tension leg platform are described, together with the model of the wind and the waves used in the following sections for the control synthesis and in the simulation experiments.

A. Model of the Wind Turbine

The mathematical model of the variable speed wind turbine is the same as in [23], [26], and [29]. The wind power is given by

$$P_{\text{wind}} = \frac{1}{2}\rho A v_{\text{in}}^3 \tag{1}$$

where ρ is the air density, v_{in} is the wind velocity actually perceived by the blades (the structure is not still), and A is the rotor swept area. Denoting by P_A the aerodynamic power captured by the wind turbine, it holds that

$$P_A = P_{\text{wind}} C_p(\lambda, \beta) \tag{2}$$

C_p is the power coefficient, β is the blade pitch angle, and λ is the tip speed ratio given by

$$\lambda = \frac{\omega_R R}{v_{\text{in}}} \tag{3}$$

where ω_R is the rotor angular speed and R is the rotor radius. The $C_p(\lambda, \beta)$ map is empirically derived from data collected either in real-world experiments or by using accurate simulation environments, such as FAST [13]. For the considered wind turbine, examples of the resulting power coefficient curves are depicted in Fig. 2 for some significant values of β. Note that, in the following, the pitch angle is defined as the complementary one with respect to that used, e.g., in FAST (which approximately ranges from 0 to 30 degrees). The aerodynamic torque is defined as

$$T_A = \frac{P_A}{\omega_R}. \tag{4}$$

In Fig. 3, a schematic representation of the wind turbine is shown: neglecting the shaft friction and assuming the rotor to be perfectly rigid, the rotor dynamics is given by

$$\tilde{J}_R \dot{\omega}_R = T_A - \tilde{T}_E \tag{5}$$

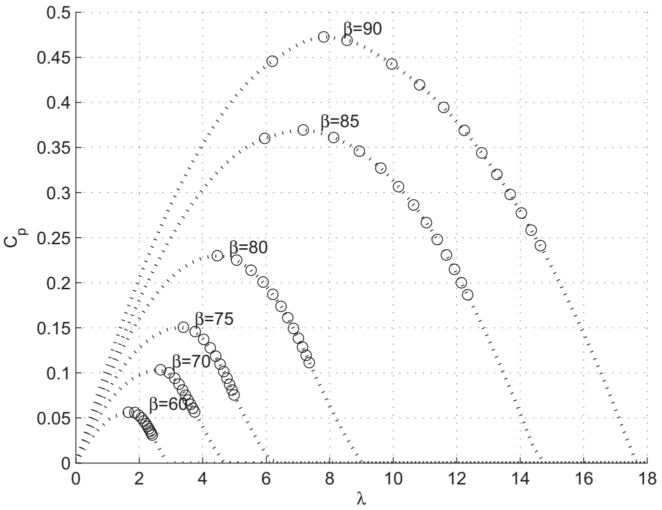

Fig. 2. Power coefficient curve. Points "o": results of simulation tests performed on FAST; dotted lines: interpolated functions.

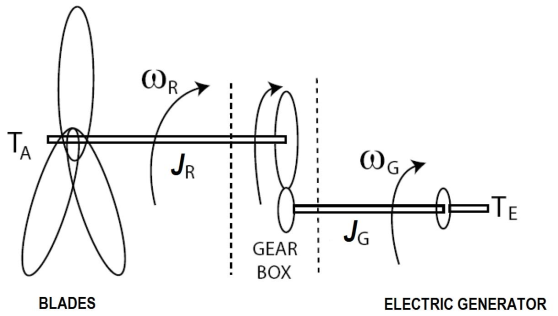

Fig. 3. Schematic representation of the wind turbine.

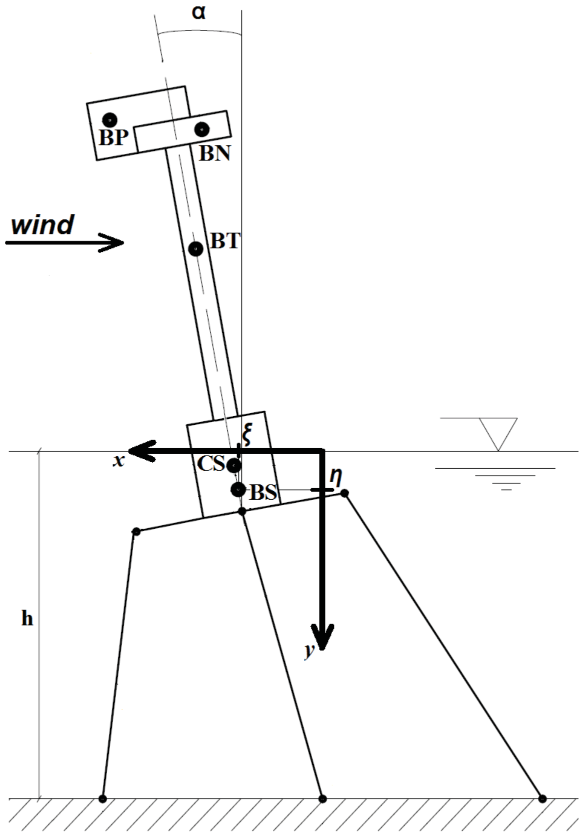

Fig. 4. Schematic 2-D representation of the tension leg platform with the wind turbine placed on it.

where $\tilde{J}_R$ is the overall inertia and $\tilde{T}_E$ is the resistant torque of the electric generator, both referred to the shaft connected to the blades

$$\tilde{J}_R = \eta_G^2 J_G + J_R \quad \tilde{T}_E = \eta_G T_E. \tag{6}$$

In (6), T_E is the generator torque, η_G is the ratio between the angular velocities of the two shafts, J_G is the sum between the inertia of the electric generator and the shaft connected to it, J_R is the sum of the inertia of the blades, of the hub, and of the shaft connected to the blades.

B. Model of the Tension Leg Platform

The model of the TLP has been derived under the following simplifying assumptions: 1) only 2-D have been considered i.e., the platform, as well as the wind turbine, is always supposed to be aligned with the wind; 2) every element of the structure and of the turbine is assumed to be rigid, and the aero-elastic effects are neglected; and 3) the wind thrust on the blades is computed through a 1-D approach. The validity of these modeling assumptions, and in particular 2) (which was *a priori* grounded on the assumption that the main motion produced by wind thrust is that related to platform pitch rather than tower bending) will be *a posteriori* assessed by analyzing the dynamic characteristics of the obtained model and through simulation experiments (see Section III), comparing the behavior of the simplified model with that of FAST.

In Fig. 4, the 2-D scheme of the offshore wind turbine is shown. The system is divided into three components.

1) Structure S: it is composed by the floater and the tower. Its center of mass is BS, while BT is the center of mass of the tower. In the computation of the wind thrust, the tower and the floater will be considered as two separated components. Finally, the point denoted CS is the center of thrust of the buoyant force.
2) Nacelle N, whose center of mass is BN.
3) Rotating part P: it is composed by the blades and the hub. Its center of mass is BP.

The coordinate system chosen to describe the wind turbine structure is shown in Fig. 4: the x-axis coincides with the water surface and its direction is opposite to the wind speed, the origin is placed in correspondence of the central anchor bolt and the y-axis is directed downward.

The state of the system is described using three coordinates: ξ, i.e., the coordinate of BS with respect to the x-axis; η, i.e., the coordinate of BS with respect to the y-axis; α, i.e., the pitch angle between the axis of the tower and the vertical direction, and their derivatives $v_\xi = \dot{\xi}$, $v_\eta = \dot{\eta}$ and $\omega = \dot{\alpha}$.

The forces acting on the system are the weight Q^{we}, the buoyancy force Q^b, the force due to the tie rods Q^t, the wind thrust Q^{wi}, the wave thrust Q^{wa}, and the hydraulic resistance Q^h (see Figs. 16–18 in the Appendix). The application of the Lagrange equations to the overall structure leads to the following system of differential equations:

$$\begin{bmatrix} 1 & 0 & 0 & 0 & 0 & 0 \\ 0 & M_X & 0 & 0 & 0 & M_d \cos\alpha \\ 0 & 0 & 1 & 0 & 0 & 0 \\ 0 & 0 & 0 & M_Y & 0 & M_d \sin\alpha \\ 0 & 0 & 0 & 0 & 1 & 0 \\ 0 & M_d \cos\alpha & 0 & M_d \sin\alpha & 0 & J_{TOT} \end{bmatrix} \begin{bmatrix} \dot{\xi} \\ \dot{v_\xi} \\ \dot{\eta} \\ \dot{v_\eta} \\ \omega \\ \dot{\omega} \end{bmatrix} = \begin{bmatrix} v_\xi \\ Q_\xi + M_d \omega^2 \sin\alpha \\ v_\eta \\ Q_\eta - M_d \omega^2 \cos\alpha \\ \omega \\ Q_\alpha \end{bmatrix} \tag{7}$$

where M_X, M_Y, M_d, and J_{TOT} are constant values, which depend on the masses and the geometries, while Q_ξ, Q_η, and Q_α are the forces expressed in the generalized coordinates (ξ, η, α), and are functions of ξ, v_ξ, $\dot{v_\xi}$, η, v_η, $\dot{v_\eta}$, α, ω, $\dot{\omega}$, of the velocity and acceleration of the water due to the waves, of the elevation of the water surface and of the wind velocity v_{in}. For simplicity of presentation, the remaining symbols that appear in (7) and the mathematical details are presented in Appendix I.

Since the structure can move, v_{in} is different from the absolute wind velocity v_w: in the point BP, in which the thrust on the blades due to the wind is assumed to be applied, it can approximately be computed as

$$v_{\text{in}} = v_w + v_\xi + d_P \omega \cos\alpha \tag{8}$$

where d_P is the distance between BS and BP.

C. Model of Wind and Waves

The wind and the waves acting on the structure have been simulated using the von Karman's model for the turbulent component of the wind speed and the Pierson–Moskowitz spectrum for the waves. The spectrum which describes the turbulent component of the wind speed [36], [37] is given by

$$S_{vK}(\omega) = \frac{0.475\sigma^2 \frac{L}{\overline{v}}}{\left[1 + \left(\frac{\omega L}{\overline{v}}\right)^2\right]^{5/6}} \tag{9}$$

where σ is the turbulence intensity, L is the correlation length of the turbulence, and $\overline{v}$ is the average wind speed. According to [37], typical values for σ belong to the interval $0.1 - 0.2$, while L usually takes values between 100 m and 330 m. Letting $\sigma = 0.17$, $L = 150$ m, and $\overline{v} = 18.5$ m/s, the resulting von Karman spectrum is shown in Fig. 5 (left side). The time-domain signal for the turbulence component of the wind speed can be obtained from von Karman spectrum using a rational filter with a white noise as input [36]. In the simulations of Section IV, the wind is generated using TurbSim [39], for comparison with FAST.

The waves have been modeled according to the linear (Airy) wave theory. The choice of the Pierson–Moskowitz spectrum for their characterization is due both to its widespread use (see, [38]) and to its simplicity, being this spectrum dependent only on a single parameter, which is a function of the mean wind speed, [38], [40]. Its spectrum is given by

$$S_{\text{PM}}(f) = \frac{\alpha_{\text{PM}} g^2}{(2\pi)^4 f^5} e^{\left[-\frac{5}{4}\left(\frac{f}{f_{\text{PM}}}\right)^{-4}\right]} \tag{10}$$

where α_{PM} is equal to 0.0081, g is the gravitational acceleration, and f_{PM} is the pick frequency, which is correlated to the mean wind speed (corresponding to an elevation of 19.5 m). Fig. 5 (right side) shows a typical spectrum plot.

A random wave signal realization can be obtained as follows. Choosing a frequency range of width Δ_f, the amplitude a_i of the monochromatic wave with angular frequency $\omega_i = 2\pi f_i$ is $a_i = \sqrt{2 S_{\text{PM}}(f_i)\Delta_f}$, where f_i is the central frequency in the interval Δ_f, while $S_{\text{PM}}(f_i)$ is the mean amplitude of the spectral density within the considered band. Dividing the whole spectrum in N frequency bands of width Δ_f, the time history of the water surface elevation at time t and position x is given by

$$\eta(x,t) = \sum_{i=1}^{N} a_i \sin(2\pi f_i t - k_i x + \varepsilon_i) \tag{11}$$

where ε_i is a random angle ranging in $[0, 2\pi)$. Parameter k_i is the wave number of the i-th monochromatic wave: in our simulations, deep water approximation [41] is valid for almost all frequencies, so that $(2\pi f_i)^2 = g k_i$, $\forall\, i$, has been considered. To obtain good results, N should be chosen greater than 200 (we set $N = 400$). As proposed in [11] and [42], the Pierson–Moskowitz spectrum has been truncated above a cut-off frequency, which is set to $3 f_{\text{PM}}$. Finally, using linear theory and deep water approximation, the kinematics of the waves in 2-D is given by

$$u_i^x(x,y,t) = \omega_i a_i e^{k_i y} \sin(\omega_i t - k_i x + \varepsilon_i) \tag{12}$$

$$u_i^y(x,y,t) = \omega_i a_i e^{k_i y} \cos(\omega_i t - k_i x + \varepsilon_i) \tag{13}$$

$$a_i^x(x,y,t) = \omega_i^2 a_i e^{k_i y} \cos(\omega_i t - k_i x + \varepsilon_i) \tag{14}$$

$$a_i^y(x,y,t) = -\omega_i^2 a_i e^{k_i y} \sin(\omega_i t - k_i x + \varepsilon_i) \tag{15}$$

where the vertical y-axis is here considered in upward direction and u_i^x, u_i^y, a_i^x, and a_i^y are the horizontal and vertical velocities and accelerations, respectively. As in (12)–(15), in deep water, the wave velocities and accelerations decrease exponentially with the distance to the surface.

D. Block Diagram of the Overall Model

The overall block diagram, including the system, the exogenous signals, and the controller is shown in Fig. 6; the inputs β and T_E are control variables, the elevation of the water surface and the velocity and acceleration of the waves are unknown disturbances. In this paper, the wind speed also is regarded as an unmeasurable disturbance but, if needed, efficient methods for obtaining reliable wind speed measurements and/or estimates are available [43]–[46]. The outputs of interest are ω_R and α and the produced power. The interaction between the wind turbine and the floating structure (see also Fig. 6) is given by the fact that (7) is used to compute ω and v_ξ appearing in (8), while (5) is used to compute ω_R, which

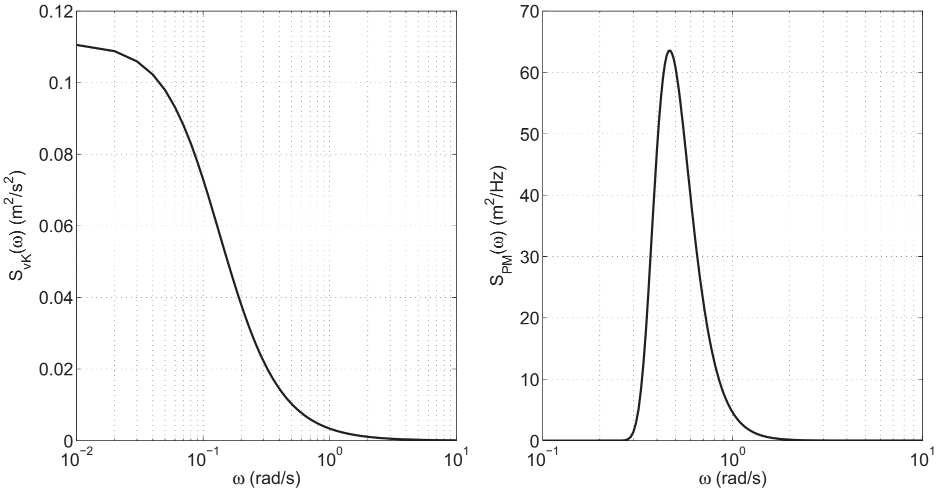

(a) (b)

Fig. 5. Von Karman spectrum of (a) the turbulence component of the wind speed and (b) Pierson–Moskowitz spectrum of the sea waves at $\overline{v} = 18.5$ m/s.

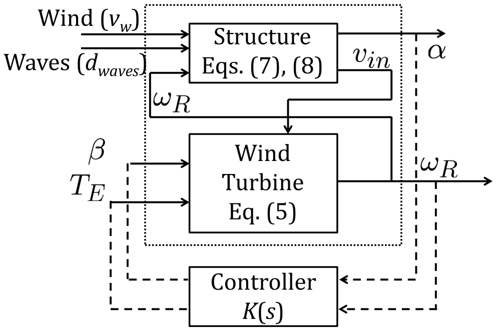

Fig. 6. Block diagram representation of the system constituted by the wind turbine and the floating structure.

in turn is used in (3) to compute λ. The latter, in combination with β, is used to compute C_p, needed in (39) to obtain v_{out}, which eventually allows one to solve (37) for evaluating the wind thrust Q^{wi}. In the model also the actuators dynamics has been initially included. Specifically, the blade pitch actuator has been modeled as a linear system whose transfer function has unitary gain and two complex conjugate poles with natural frequency 5.0265 rad/s and damping coefficient 0.8 [29] and [47]. The model of the electric generator has been represented by a very fast first-order system with unitary gain and time constant equal to 0.002 [48]. Due to their fast dynamics, and since their inclusion does not significantly affect the simulation results, these actuators have not been considered in the simulations reported in Section IV, consistently with FAST.

III. PARAMETER TUNING

The parameters used in the simulations have been derived from [13] for the turbine and the support structure, and from [49] for standard fluidodynamic-related parameters: their values are listed in Appendix II. A tuning procedure for some additional model parameters has been carried out comparing the results provided by the simulator with those of the complete 3-D reference simulation tools FAST. In particular:

1) $C_p(\lambda, \beta)$ has been estimated by simulating the static responses of a non-controlled on-land turbine for different constant values of β and T_E, selected in order to explore the largest possible range of values of λ, see Fig. 2.
2) The constant added mass of the floating platform in horizontal direction m_x (see Appendix I) has been identified via simulation comparison where, at time $t = 0$ (and for different constant values of β and T_E), and steps in the wind speed have been applied to the offshore wind turbine, so as to generate relative motion between the water and the floater.
3) The additive thrust correction term ΔFA (see Appendix I), incorporating some phenomena which have not been accounted for in our simplified model, has been identified using the same procedure as in the case of m_x. Specifically, an horizontal force acting on BP has been added, in order to achieve, in stationary conditions, the same results of the reference simulator.

The computed values of these parameters are reported in Appendixes I and II.

Validation plots, comparing the simulation results obtained using the identified simplified model and the reference one, are shown in Figs. 7 and 8. Importantly, both in the identification and the in the validation simulations, all the degrees of freedom available in FAST were enabled. The system is in initial stationary conditions with $\beta = 80°$, $v_w = 18$ m/s, and $\tilde{T}_E = 4.18$ MNm. Fig. 7 shows the step and ramp variations applied to the inputs v_w, β, and $\tilde{T}_E$, which are representative of realistic range variations in standard working conditions, while in Fig. 8 the corresponding outputs ξ, η, α obtained with the reference model FAST and with the simplified one are given. The transients reported in Fig. 8 show very good agreement of the two responses, in terms of both static and dynamic conditions, as also witnessed by the results reported in Table I. These results, together with those described in the following section, witness the validity of the modeling assumptions previously introduced.

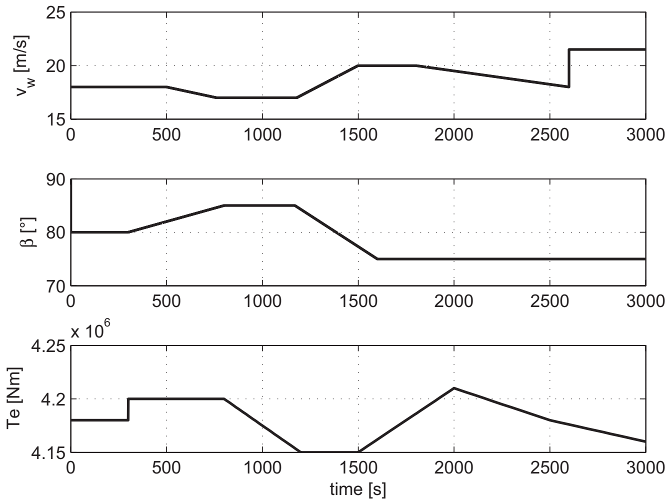

Fig. 7. Values of the input variables v_w and β used in the open-loop tests.

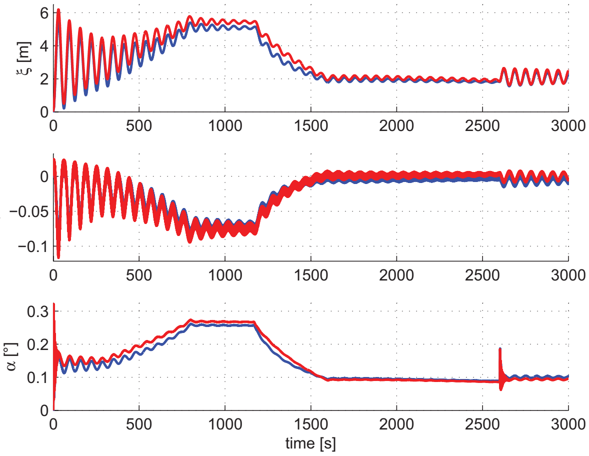

Fig. 8. Comparison of the open-loop outputs (i.e., variables ξ, η, α) obtained with FAST (blue lines) and with the simplified model (red lines).

TABLE I

SUMMARY OF COMPARISON RESULTS OF THE SIMPLIFIED SIMULATOR: MEAN VALUES AND STANDARD DEVIATION OF ξ, η, AND α COMPARED TO THE CORRESPONDING VALUES OBTAINED USING FAST

	Simplified Simulator	FAST
Mean(ξ) (m)	3.13	2.86
Std(ξ) (m)	1.39	1.27
Mean(η) (m)	−0.02	−0.02
Std(η) (m)	0.03	0.03
Mean(α) (°)	0.15	0.14
Std(α) (°)	0.07	0.06

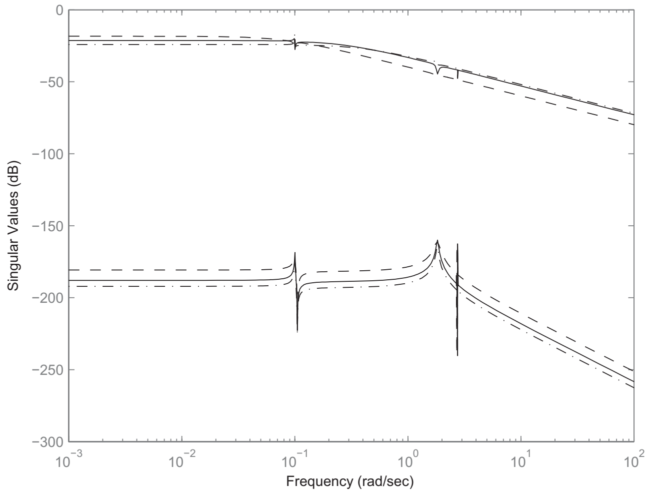

Fig. 9. Singular values of the linearized system at v_w = 13 m/s (dashed lines), v_w = 18 m/s (solid lines), and v_w = 23 m/s (dash-dot lines). Upper bode diagrams: maximum singular values; lower bode diagrams: minimum singular values.

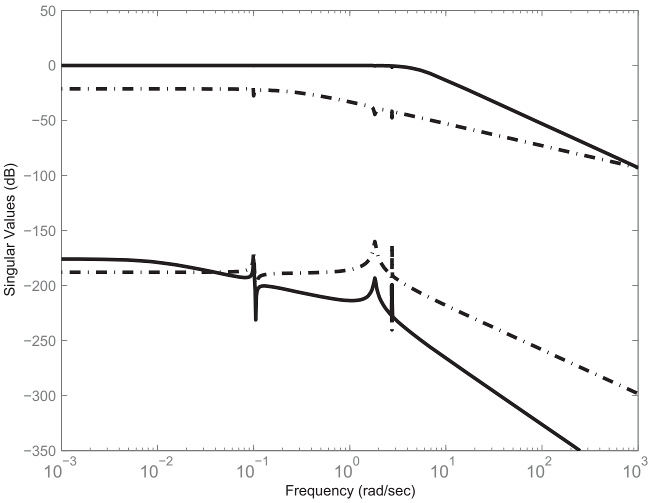

Fig. 10. Singular values of the open-loop system (dashed-dotted line) and of the complementary sensitivity function (solid line).

IV. CONTROL STRATEGIES

A regulator has been designed for control of the rotor angular speed ω_R and of the pitch angle α in Region R3 by acting on the input variables T_E and β, see Fig. 6.

A preliminary analysis of the linearized model of the overall system has been performed at different wind speeds, see Fig. 9 where the input/output singular values of the system at v_w=13 m/s, v_w=18 m/s, and v_w=23 m/s are reported. The plots in Fig. 9 show that only small variations of the gain occur at different operating conditions. Therefore, a robust invariant controller can provide satisfactory results in the whole operating range. For this reason, the regulator has been designed for the linear system computed at $v_{\text{in}} = 18$ m/s and linear H_∞ control [18] and [19] has been used in view of its capability to guarantee robust asymptotic stability and to minimize the effect of disturbances.

In order to synthetically describe the adopted control approach, and with reference to the linearized system, denote by $G(s)$ the transfer function between the control vector $[\beta \ T_E]'$ and the controlled variables $[\alpha \ \omega_R]'$, let $K(s)$ be the regulator transfer function (see Fig. 6), and define by $S(s) = (I + G(s)K(s))^{-1}$ and $T(s) = (I + G(s)K(s))^{-1}G(s)K(s)$ the sensitivity and the complementary sensitivity transfer functions. Then, according to the H_∞ approach, $K(s)$ is computed

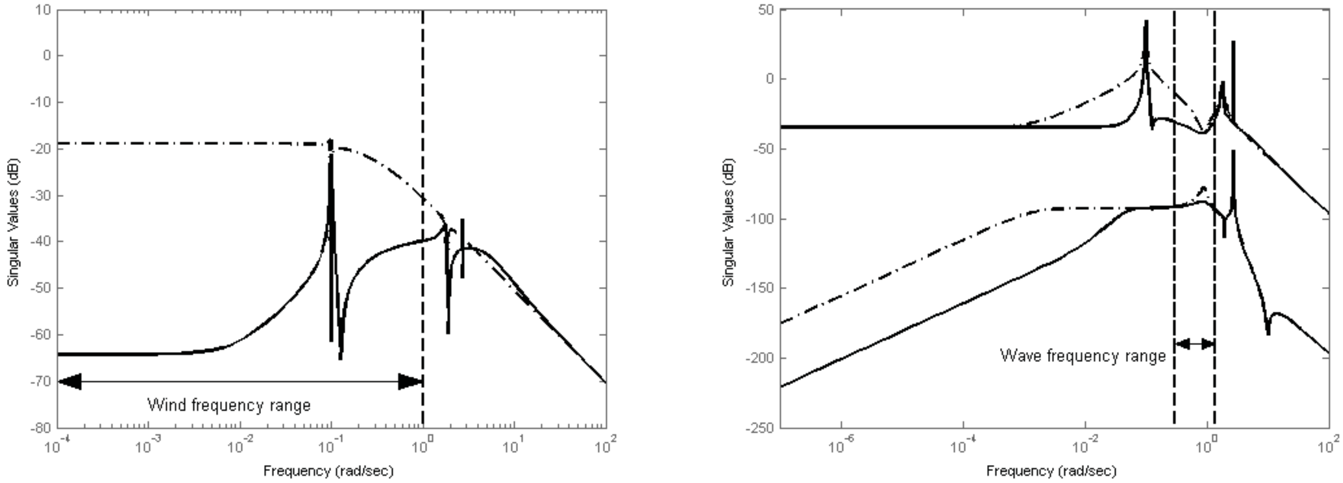

Fig. 11. Singular values of the open-loop (dashed-dotted line) and closed-loop (solid line) transfer functions between (left) the wind and (right) the waves and the controlled variables. The indicated intervals represent the frequency ranges where the spectrum of the disturbances is significant.

by solving the optimization problem

$$\min_{K(s)} \left\| \begin{bmatrix} W_1(s)S(s) \\ W_2(s)K(s)S(s) \\ W_3(s)T(s) \end{bmatrix} \right\|_\infty \tag{16}$$

where the shaping functions $W_1(s)$, $W_2(s)$, and $W_3(s)$ are design parameters, which must be selected to meet specific control objectives. The stated optimization problem is tantamount to requiring that $W_1(j\omega)S(j\omega)$, $W_2(j\omega)K(j\omega)S(j\omega)$, and $W_3(j\omega)T(j\omega)$ "be small for all frequencies" [50], under the constraints imposed by the system's dynamics (e.g., $S(s)+T(s) = I$). In turn this means that $W_1(s)$, $W_2(s)$, and $W_3(s)$ can be seen as the inverses of the desired functions $S(s)$, $K(s)S(s)$, and $T(s)$, respectively. Now recall that in the considered application the main goal of the control design is to reject the effect of the wind and waves, i.e., of the disturbances acting on the system. This can be achieved provided that the closed-loop transfer function between the disturbances $[v_w \ d_{\text{waves}}]'$ and the output vector $[\alpha \ \omega_R]'$ guarantees sufficient attenuation up to 1 rad/s, where the spectra of these disturbances have significant components, see Figs. 5 and 11. In this respect, note that the closed-loop transfer function between the disturbances $[v_w \ d_{\text{waves}}]'$ and the output vector $[\alpha \ \omega_R]'$ is the cascade, including the sensitivity function and the open-loop transfer function between the disturbances and the output. Furthermore, concerning the choice of considering, in the operating region R3, ω_R as a controlled output rather than P_E, the rationale is similar to the one applied in [10], where the generator torque is kept constant for minimizing the drive train loads and for reducing the pitch activity, and ω_R is controlled by acting on the blade pitch angle. The component of $W_3(s)$ associated to the input T_E will be therefore selected in such a way that its deviation with respect to the nominal value is limited. The above considerations lead to select $W_1(s) = (1000/100s + 1)I_2$, I_2 being the 2×2 identity matrix, which guarantees 20 dB attenuation at $\omega = 1$ rad/s; correspondingly, and in order to have consistent specifications on the required bandwidth imposed on $T(s)$, it has been set $W_3(s) = (0.01s + 0.001/0.01s + 1)I_2$. Finally, after an accurate tuning procedure, the control sensitivity weight has been chosen as $W_2(s) = 0.1I_2$, so as to have a limited control action.

The open-loop and closed-loop singular values, and the singular values of the open-loop and closed-loop transfer functions between the wind, the waves, and the controlled variables are illustrated in Figs. 10 and 11. These figures clearly show the attenuation effects of the closed-loop system with respect to the wind fluctuations and the waves in the frequency bands where these signals have significant components.

A. Simulation Results

The H_∞ regulator has been used for control of the simplified model and of the FAST simulator, both affected by the same wind realization, shown in Fig. 12. Note that the wind speed variations are in the range 12–25 m/s and cover the whole R3 region.

As for the waves, it has not been possible to use the same signal. However, two different realizations generated by means of the same Pierson-Moskovitz spectrum (see Section II-C) have been used in the two simulation environments. The realization of the water surface elevation with respect to still water depth and taken at point $x = 0$ m, applied to the model described in this paper, is depicted in Fig. 12.

Fig. 13 shows the trajectory of the rotor speed, of the electrical power, and of the pitch angle computed with the simplified model and with FAST, while the corresponding mean values and root mean square errors (RMSE) are summarized in Table II. The results achieved show that the performance of the regulator in the two simulation environments are comparable, so that it is possible to conclude that the simplified simulation model can be efficiently used in the controller design phase. Again, higher frequency modes of FAST generate higher frequency oscillations.

Finally, the performance of the H_∞ regulator have been compared with those of the gain scheduled PI controller (PI$_{gs}$) described in [7] and available in the FAST environment. In Fig. 14, the trajectories of the rotor speed, of the electrical

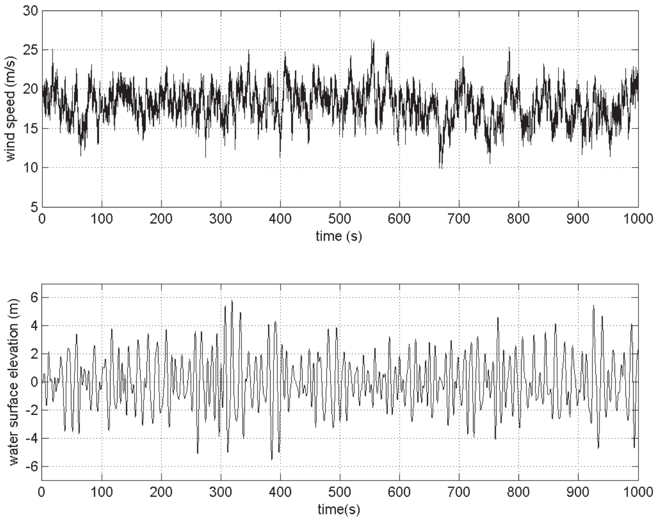

Fig. 12. Wind speed and water surface elevation used in the simulations.

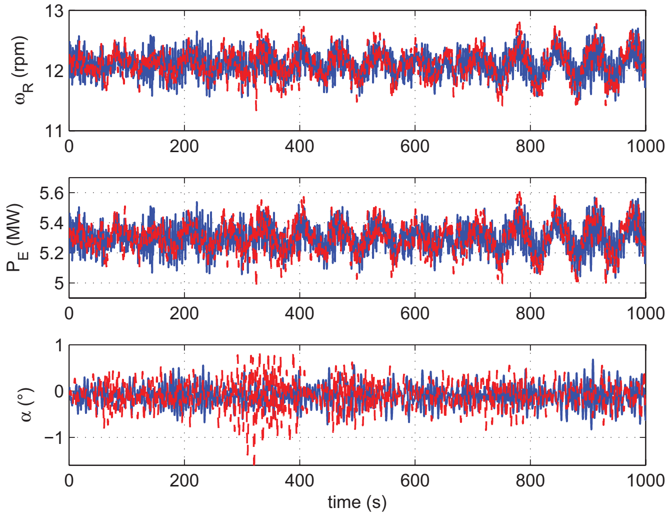

Fig. 13. Rotor speed, produced electrical power, and pitch angle obtained using the H_∞ regulator applied to the simplified simulator (red dashed lines) and to FAST (blue lines).

TABLE II

SUMMARY OF H_∞ CONTROLLER PERFORMANCE ON FAST AND ON THE SIMPLIFIED SIMULATOR: MEAN VALUES AND ROOT MEAN SQUARE ERRORS OF ω_R AND α

	Simplified simulator	FAST
Mean(P_E) (MW)	5.2974	5.2972
RMSE(P_E) (MW)	0.1025	0.0858
Mean(ω_R) (rpm)	12.102	12.101
RMSE(ω_R) (rpm)	0.2341	0.1960
Mean(α) (°)	−0.088	−0.095
RMSE(α) (°)	0.300	0.228

TABLE III

SUMMARY OF H_∞ AND PI_{gs} CONTROLLER PERFORMANCES ON FAST: MEAN VALUES AND ROOT MEAN SQUARE ERRORS OF ω_R AND α

	PI_{gs}	H_∞
Mean(P_E) (MW)	5.296	5.297
RMSE(P_E) (MW)	0.070	0.086
Mean(ω_R) (rpm)	12.114	12.101
RMSE(ω_R) (rpm)	0.579	0.196
Mean(α) (°)	−0.094	−0.095
RMSE(α) (°)	0.166	0.228

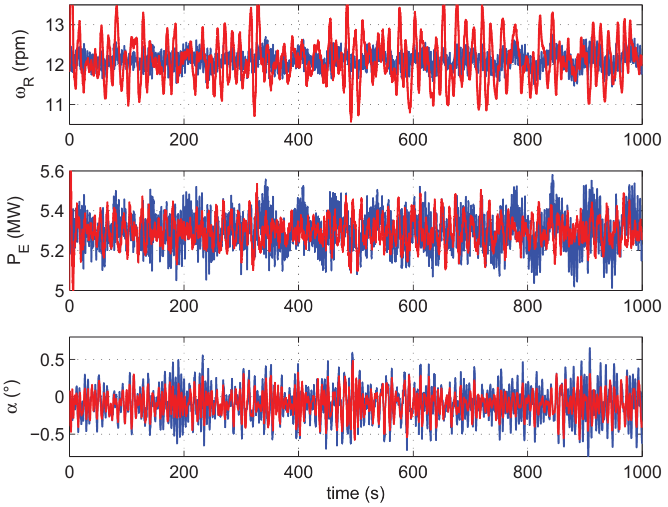

Fig. 14. Rotor speed, produced electrical power, and pitch angle obtained using H_∞ controller (blue lines) and PI_{gs} controller (red lines), both applied to FAST.

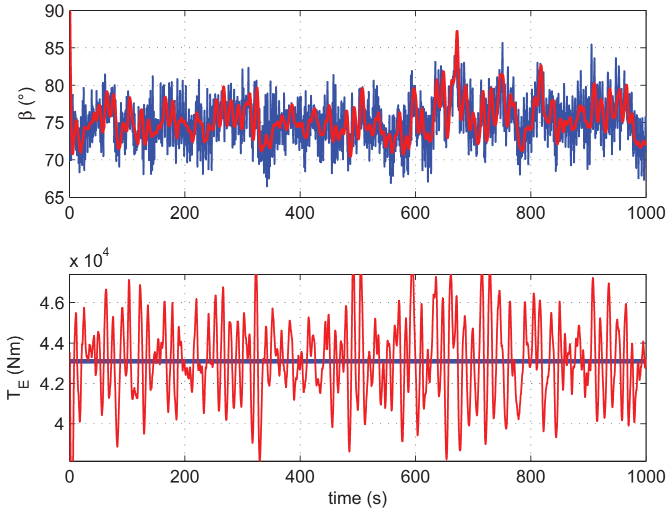

Fig. 15. Blades pitch angle and generator torque used with H_∞ controller (blue lines) and PI_{gs} controller (red lines) applied to FAST.

power, and of the pitch angle computed in the FAST environment are depicted for both regulators. In these tests, the H_∞ controller leads to an improvement in the regulation of the rotor speed while the produced power and the pitch angle undergoes slightly larger oscillations. These conclusions are also highlighted by the results reported in Table III.

The applied inputs are depicted in Fig. 15, while their mean values and standard deviations are reported in Table IV: the H_∞ controller requires faster changes in β, but still compatible with the dynamics of the blades actuators described, e.g.,

TABLE IV

SUMMARY OF H_∞ AND PI$_{gs}$ CONTROLLER PERFORMANCES ON FAST: MEAN VALUES AND STANDARD DEVIATIONS (STD) OF THE APPLIED INPUTS

	PI$_{gs}$	H_∞
Mean(T_E) (kNm)	43.13	43.09
Std(T_E) (Nm)	1933	0.0016
Mean(β) (°)	75.32	75.17
Std(β) (°)	2.40	2.88

in [48], [51]. The usage of the electric torque, on the contrary, is limited to very small variation for the H_∞ controller if compared to those needed by the PI$_{gs}$ one (the scale of Fig. 15 makes such small variations to generate a straight line).

V. CONCLUSION

In this paper, a simplified, 2-D model of an offshore wind turbine with tension leg platform was described. It was suited for analysis and control and, after a simple tuning procedure, it was shown to be consistent with the widely used, complete 3-D simulator FAST. Thanks to its simplicity, its direct implementation in programming languages, such as Fortran or C can lead to very fast simulations, a non-negligible advantage when different regulators must be tuned and compared, for example via MonteCarlo experiments. It was also shown that a regulator designed for the simplified model can be directly applied to a 3-D, highly complex simulator without any performance degradation. The results achieved encourage extending the adopted control-oriented approach to other floating platforms. Future research will also include further tests on the proposed controller, encompassing a statistical approach with a larger statistical basis and a thorough analysis of fatigue loads.

APPENDIX I

In this Appendix, the equations of the mathematical model of the tension leg structure (7) are presented. The forces acting on the system are the weight Q^{we}, the buoyancy force Q^b, the tie rod force Q^t, the wind force Q^{wi}, the force due to the waves Q^{wa} and the hydraulic drag Q^h. Each of these components will be derived in the following.

Weight Forces: The weight of the three components of the overall system, applied in their centers of mass, represent three forces aligned with the y-axis (Fig. 16). The components, with respect to the generalized coordinates, are

$$Q_\xi^{we} = 0 \tag{17}$$

$$Q_\eta^{we} = (M_N + M_P + M_S)g \tag{18}$$

$$\begin{aligned} Q_\alpha^{we} &= [(M_N d_{Nv} + M_P d_{Pv})\sin\alpha \\ &\quad + (M_N d_{Nh} + M_P d_{Ph})\cos\alpha]g \end{aligned} \tag{19}$$

where M_N, M_P, and M_S are the masses of the systems N, P, and S, respectively, and d_{Nv}, d_{Pv}, d_{Nh}, and d_{Ph} are the distances between BS and BN and between BS and BP in the direction parallel to the tower's axis (subscript "v") and perpendicular to it (subscript "h"), respectively. The corresponding total distances are $d_N = \sqrt{d_{Nh}^2 + d_{Nv}^2}$, between BS and BN, and $d_P = \sqrt{d_{Ph}^2 + d_{Pv}^2}$), between BS and BP. The weights of the tie rods are added to their elastic forces.

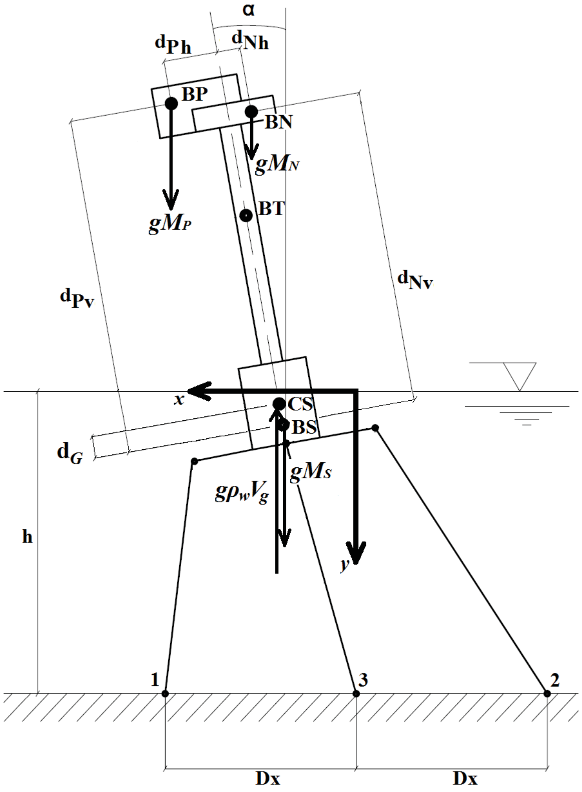

Fig. 16. Schematic 2-D representation of the weights and of the buoyant force acting on the structure.

Buoyancy Forces: The buoyancy force is aligned with the y-axis, it is an upward force applied in the center of thrust CS (see Fig. 16). The three components are

$$Q_\xi^b = 0 \tag{20}$$

$$Q_\eta^b = -\rho_w V_g g \tag{21}$$

$$Q_\alpha^b = \rho_w V_g g \, d_G \sin\alpha \tag{22}$$

where ρ_w is the water density, V_g is the submerged volume of the floater, and d_G is the distance between BS and CS. V_g depends on the position of the structure and on the elevation of the water surface. To approximate the depth of water, the surface elevation is evaluated at three points: $x = \xi$, $x = \xi + r_g$, and $\xi - r_g$, where r_g is the radius of the floating structure. Then, it is assumed the water surface where the structure is located to be flat and horizontal, with a depth h_w equal to the average of the three points mentioned above. In this way, since $\cos(\alpha) \simeq 1$, a good approximation of the height of the submerged part of the floating structure is given by

$$h_{\text{sub}} = \min((h_w - h + \eta + d_{S\text{bott}}), h_{pt}) \tag{23}$$

where h is the water depth without waves, $d_{S\text{bott}}$ is the vertical distance between BS and the bottom of the structure, and h_{pt} it the height of the floating structure. Then, V_g is computed as

$$V_g = h_{\text{sub}} \pi r_g^2 + \max(((h_w - h + \eta + d_{S\text{bott}}) - h_{pt}), 0)\pi r_{tb}^2. \tag{24}$$

TABLE V

MAIN PARAMETERS OF THE OFFSHORE WIND TURBINE (1)

Parameter	**Description**	**Value**		**Source**
A	Rotor area	12469	m^2	[13]
A_N	Nacelle area	9.62	m^2	[13]
C_Δ	Coefficient for computing ΔFA	10207305.54	-	Identification
$C_{dg\parallel}$	Parallel cylinder drag coefficient	0.006	-	[49]
$C_{dg\perp}$	Perpendicular cylinder drag coefficient	1	-	[49]
C_{dgb}	Floater bottom drag coefficient	1.9	-	[49]
C_{dN}	Nacelle drag coefficient	1	-	[49]
C_{dT}	Tower drag coefficient	1	-	[49]
D_x	Distance between anchor bolts	27	m	[13]
d_{Nh}	Horizontal distance between BS and BN	-1.8	m	[13]
d_{Nv}	Vertical distance between BS and BN	126.9003	m	[13]
d_{Ph}	Horizontal distance between BS and BP	5.4305	m	[13]
d_{Pv}	Vertical distance between BS and BP	127.5879	m	[13]
$d_{S\text{bott}}$	Vertical distance between BS and floater bottom	10.3397	m	[13]
d_T	Vertical distance between BS and BT	75.7843	m	[13]
d_t	Vertical distance between BS and hooks of tie rods	10.3397	m	[13]
η_G	Speed ratio between high and low speed shafts	97	-	[13]
F_Δ	Coefficient for computing ΔFA	$\begin{bmatrix} -22790.37 & -279533.43 \end{bmatrix}$	-	Identification
g	Standard gravity	9.80665	m/s^2	[13]
H_Δ	Coefficient for computing ΔFA	$\begin{bmatrix} -2613.44 & 810.13 \\ 810.13 & 1744.28 \end{bmatrix}$		Identification
h	Depth of water	200	m	[13]
h_{pt}	Height of the floating structure	47.89	m	[13]
J_G	Total inertia of electric generator and high speed shaft	534.116	kg m^2	[13]
J_N	Nacelle moment of inertia	2607890	kg m^2	[13]
J_P	Blades, hub and low speed shaft moment of inertia	50.365	kt m^2	[13]
J_R	Total inertia of blades, hub and low speed shaft	35444067	kg m^2	[13]
J_S	"Structure" moment of inertia	3.4917	Mt m^2	[13]
$K_{T1,2}$	Spring constant of lateral tie rods	$2(1.5/l_0)$	GN/m	[13]
K_{T3}	Spring constant of central tie rod	$4(1.5/l_0)$	GN/m	[13]
l_0	Rest length of tie rods	151.73	m	[13]
l_a	Distance between the hooks of tie rods	27	m	[13]

The second term in (24) accounts for the possibility of having a small portion of the tower submerged by the water: r_{tb} is the radius of the lowest part of the tower. The parameter d_G is approximated as

$$d_G = \eta - h_{\text{sub}}/2 \tag{25}$$

Tie Rod Forces: The ith tie rod, $i = 1, 2, 3$, has been modeled as a spring whose traction, applied to the structure, is given by

$$f_i = \max(0, K_{Ti}(l_i - l_0)) \tag{26}$$

where l_0 is the rest length of the tie rods and K_{Ti} is the spring constant of the ith tie rod. The lengths of the three tie rods, see Fig. 18, are

$$\begin{aligned} l_1 &= \sqrt{(h-\eta-l_a\sin\alpha-d_t\cos\alpha)^2+(D_x-\xi-l_a\cos\alpha+d_t\sin\alpha)^2} \\ l_2 &= \sqrt{(h-\eta+l_a\sin\alpha-d_t\cos\alpha)^2+(D_x+\xi-l_a\cos\alpha-d_t\sin\alpha)^2} \\ l_3 &= \sqrt{(h-\eta-d_t\cos\alpha)^2+(\xi-d_t\sin\alpha)^2} \end{aligned} \tag{27}$$

where d_t is the vertical distance between BS and the point of the floater where the tie rods are hooked, D_x is the distance between the anchor bolts, and l_a is the horizontal distance between the hooks on the floater. Note that, according to the common layout of TLPs, $D_x = l_a$. The tie rod forces, including the contributions of the weights, are

$$Q_\xi^t = f_1\sin\theta_1 - f_2\sin\theta_2 - f_3\sin\theta_3 \tag{28}$$

$$Q_\eta^t = f_1\cos\theta_1 + f_2\cos\theta_2 + f_3\cos\theta_3 + 4\lambda_{tir}l_0 \tag{29}$$

$$\begin{aligned} Q_\alpha^t = {} & f_1[l_a\cos(\theta_1+\alpha) - d_t\sin(\theta_1+\alpha)] \\ & - f_2[l_a\cos(\theta_2-\alpha) - d_t\sin(\theta_2-\alpha)] \\ & + f_3 d_t\sin(\theta_3-\alpha) + \lambda_{tir}l_0 \\ & \times[l_a\cos(\alpha) - d_t\sin(\alpha)] \\ & - \lambda_{tir}l_0[l_a\cos(\alpha) \\ & + d_t\sin(\alpha))] - 2\lambda_{tir}l_0 d_t\sin(\alpha) \end{aligned} \tag{30}$$

where

$$\theta_1 = \arctan\frac{(D_x-\xi-l_a\cos\alpha+d_t\sin\alpha)}{(h-\eta-l_a\sin\alpha-d_t\cos\alpha)} \tag{31}$$

TABLE VI

MAIN PARAMETERS OF THE OFFSHORE WIND TURBINE (2)

M_N	Mass of nacelle	240000	kg	[13]
M_P	Mass of blades and hub	110000	kg	[13]
M_S	Mass of “structure” (tower and floater)	8947870	kg	[13]
m_x	Added mass in horizontal direction	11.127	kt	Identification
m_y	Added mass in vertical direction	1.5044	kt	[13]
n_{dg}	Number of floater sub-cylinders	2	-	-
$\overline{\omega}_R$	Rotor rated speed	12.1	rpm	[13]
$\overline{P}_M$	Rated mechanical power	5.29661	MW	[13]
R	Radius of rotor	63	m	[13]
r_g	Radius of floater	9	m	[13]
r_{lb}	Maximum radius of the tower	3	m	[13]
ρ	Density of air	1.225	kg/m^3	[13]
ρ_w	Density of water	1025	kg/m^3	[13]
$v_{\text{cut-in}}$	Wind turbine cut-in wind speed	3	m/s	[13]
v_{rated}	Wind turbine rated wind speed	11.4	m/s	[13]
$v_{\text{cut-off}}$	Wind turbine cut-off wind speed	25	m/s	[13]

TABLE VII

STATES AND INPUTS OF THE OFFSHORE WIND TURBINE MODEL

Variables	**Description**
α	Structure pitch angle.
β	Blades pitch angle.
η	Vertical position of BS.
ξ	Horizontal position of BS.
ω_R	Low-speed shaft angular velocity.
ω	$\dot{\alpha}$.
T_E	Generator resistant torque.
v_η	$\dot{\eta}$.
v_ξ	$\dot{\xi}$.

TABLE VIII

DISTURBANCES AND FORCES ACTING ON THE OFFSHORE WIND TURBINE

Disturbances	**Description**
v_w	Absolute wind velocity.
η	Water surface elevation.
u^x	Water horizontal velocity.
u^y	Water vertical velocity.
a^x	Water horizontal acceleration.
a^y	Water vertical acceleration.
Q^b	Buoyancy force.
Q^h	Hydraulic drag.
Q^t	Tie rod force.
Q^{wa}	Waves force.
Q^{we}	Weight.
Q^{wi}	Wind force.

$$\theta_2 = \arctan\frac{(D_x + \xi - l_a\cos\alpha - d_t\sin\alpha)}{(h - \eta + l_a\sin\alpha - d_t\cos\alpha)} \quad (32)$$

$$\theta_3 = \arctan\frac{(\xi - d_t\sin\alpha)}{(h - \eta - d_t\cos\alpha)} \quad (33)$$

Wind Forces: For simplicity, the wind thrust has been studied according to a 1-D approach, assuming the wind speed to be the same in every point of the wind turbine. In addition, the thrust has been modeled with three horizontal point forces (FA, FAN, and FAT) applied in BP, BN, and BT (see Fig. 17), respectively. Given the values of FA, FAN, and FAT, the component of the forces with respect to the free coordinates are

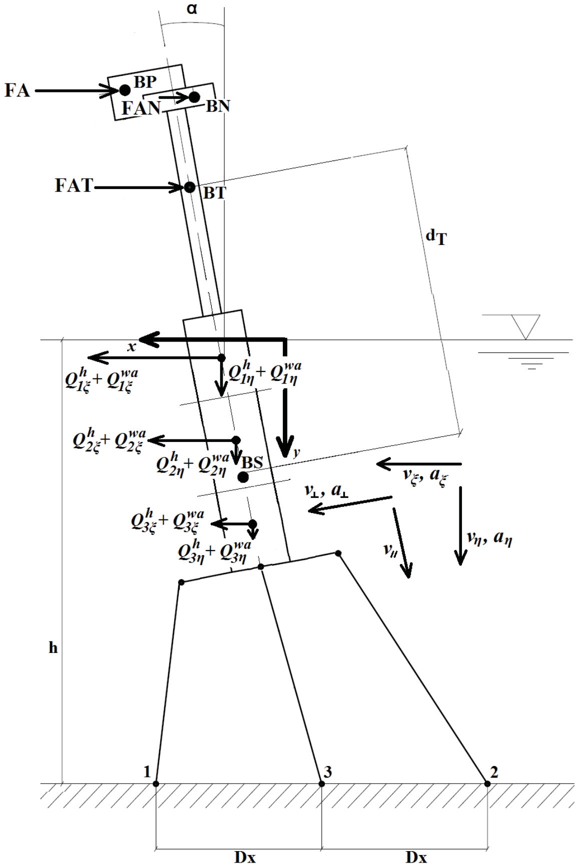

Fig. 17. Schematic 2-D representation of the aerodynamic thrust and of the forces due to the interaction with the water acting on the structure.

$$Q^{wi}_\xi = -(\text{FA} + \text{FAN} + \text{FAT}) \quad (34)$$

$$Q^{wi}_\eta = 0 \quad (35)$$

$$\begin{aligned} Q^{wi}_\alpha &= -\text{FA}(d_{Pv}\cos\alpha - d_{Ph}\sin\alpha) \\ &\quad -\text{FAN}(d_{Nv}\cos\alpha - d_{Nh}\sin\alpha) \\ &\quad -\text{FAT}d_T\cos\alpha \end{aligned} \quad (36)$$

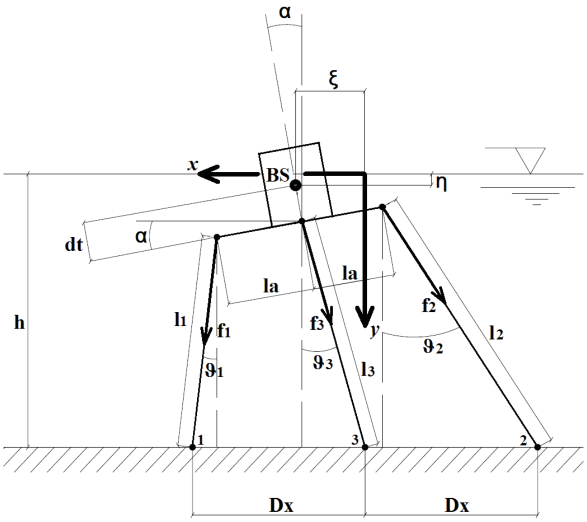

Fig. 18. Schematic 2-D representation of the forces due to the tie rods acting on the structure.

where d_T is the distance between BS and BT. FA is computed as [29]

$$\mathrm{FA} = \frac{1}{2}\rho A (v_{\text{in}}^2 - v_{\text{out}}^2) + \Delta\mathrm{FA} \tag{37}$$

where $\Delta\mathrm{FA}$ is an additive thrust correction term. The function $\Delta\mathrm{FA}(\beta, v_{\text{in}})$ has been identified using the reference simulator FAST, and takes the form

$$\Delta\mathrm{FA} = [v_{\text{in}}, \beta] H_\Delta [v_{\text{in}}, \beta]^T + F_\Delta [v_{\text{in}}, \beta]^T + C_\Delta \tag{38}$$

where the coefficients H_Δ, F_Δ, and C_Δ are specified in Appendix II.

In (37), v_{out} is the wind speed after the rotor. Through simple substitutions in (2), it holds that

$$v_{\text{out}}^3 + v_{\text{in}} v_{\text{out}}^2 - v_{\text{in}}^2 v_{\text{out}} - (1 - 2C_p) v_{\text{in}}^3 = 0 \tag{39}$$

The terms FAN and FAT are proportional to the relative speed between the wind and the points BN and BT, where they are applied, and are given by

$$\mathrm{FAN} = \frac{1}{2}\rho C_{dN} A_N \cos(\alpha)(v_w + v_\xi + d_N \omega \cos\alpha)^2 \tag{40}$$

$$\mathrm{FAT} = \frac{1}{2}\rho C_{dT} h_T D_T \cos(\alpha)(v_w + v_\xi + d_T \omega \cos\alpha)^2 \tag{41}$$

where C_{dN} and C_{dT} are the drag coefficients of the system N and of the tower, h_T and D_T are the tower's height and mean diameter, while A_N is the frontal section of system N. In (40) and (41), (8) is used to compute the relative speed between the wind and the points BN and BT.

Wave and Drag Forces: The wave thrust and the hydraulic drag are computed decomposing the cylindrical floater in vertical direction in n_{dg} sub-cylinders with the same transverse section of the floating structure, each one representing a "slice" of the overall floater. For each sub-cylinder, the hydrodynamic forces are computed by means of the Morison equations (see [52]), using the kinematics of the undisturbed water particles evaluated at the geometric center of each sub-cylinder. The sum of these forces is taken as the overall force acting on the floating structure. To implement the exposed strategy, first of all the relevant kinematics of the water particles is computed in direction parallel and perpendicular to the axis of the floater with the following equations:

$$\begin{aligned} v_{i\perp} &= [v_\xi + (h_{ipg} - d_{S\text{bott}})\omega\cos(\alpha) - v_{ix}]\cos(\alpha) \\ &\quad + [v_\eta + (h_{ipg} - d_{S\text{bott}})\omega\sin(\alpha) - v_{iy}]\sin(\alpha) \end{aligned} \tag{42}$$

$$\begin{aligned} v_{i\|} &= [v_\xi + (h_{ipg} - d_{S\text{bott}})\omega\cos(\alpha) - v_{ix}]\sin(-\alpha) \\ &\quad + [v_\eta + (h_{ipg} - d_{S\text{bott}})\omega\sin(\alpha) - v_{iy}]\cos(\alpha) \end{aligned} \tag{43}$$

$$a_{i\perp} = a_{ix}\cos(\alpha) + a_{iy}\sin(\alpha) \tag{44}$$

In (42)–(44), $v_{i\perp}$ and $a_{i\perp}$ are the relative velocity between the water and the immersed body and the acceleration of the water, respectively, evaluated at the center of i-th cylinder, projected in direction perpendicular to the axis of the floater; $v_{i\|}$ is the relative velocity between the water and the immersed body, evaluated at the center of i-th cylinder, projected in direction parallel to the axis of the floater. h_{ipg} is the distance of the geometric center of the i-th cylinder from the bottom of the floater ($h_{ipg} = (i - 0.5)h_{\text{sub}}/n_{dg}$); v_{ix}, v_{iy}, a_{ix}, and a_{iy} are the horizontal and vertical component of the water velocity and the horizontal and vertical component of the water acceleration evaluated at the geometric center of the i-th cylinder, respectively. It is possible to compute the hydraulic drag in x direction acting on the i-th cylinder $Q_{i\xi}^h$ as

$$\begin{aligned} Q_{i\xi}^h = &-\tfrac{1}{2} C_{dg\perp} \rho_w (2r_g)(h_{\text{sub}}/n_{dg}) |v_{i\perp}| v_{i\perp} \cos(\alpha) \\ &-\tfrac{1}{2} C_{dg\|} \rho_w \pi (2r_g)(h_{\text{sub}}/n_{dg}) |v_{i\|}| v_{i\|} \sin(\alpha) \end{aligned} \tag{45}$$

where $C_{dg\perp}$ and $C_{dg\|}$ are the drag coefficients of every cylinder in direction perpendicular and parallel to its axes, respectively. The hydraulic drag in y direction acting on the i-th cylinder $Q_{i\eta}^h$ is

$$\begin{aligned} Q_{i\eta}^h = &-\tfrac{1}{2} C_{dg\perp} \rho_w (2r_g)(h_{\text{sub}}/n_{dg}) |v_{i\perp}| v_{i\perp} \sin(\alpha) \\ &-\tfrac{1}{2} C_{dg\|} \rho_w \pi (2r_g)(h_{\text{sub}}/n_{dg}) |v_{i\|}| v_{i\|} \cos(\alpha) \end{aligned} \tag{46}$$

while the components $Q_{i\xi}^{wa}$ and $Q_{i\eta}^{wa}$ of the wave thrust applied in the center of the i-th cylinder and aligned with the x-axis and y-axis are

$$Q_{i\xi}^{wa} = (\rho_w V_g + m_x) a_{i\perp} \cos(\alpha)/n_{dg} \tag{47}$$

$$Q_{i\eta}^{wa} = (\rho_w V_g + m_x) a_{i\perp} \sin(\alpha)/n_{dg}. \tag{48}$$

The terms proportional to the accelerations of the structure are considered in the computation of the system's Lagrange equations, so here they have been neglected. The resulting total forces are

$$Q_\xi^h = \sum_{i=1}^{n_{dg}} Q_{i\xi}^h - \frac{1}{2} C_{dgb} \rho_w \pi r_g^2 |v_{I\|}| v_{I\|} \sin(\alpha) \tag{49}$$

$$Q_\eta^h = \sum_{i=1}^{n_{dg}} Q_{i\eta}^h - \frac{1}{2} C_{dgb} \rho_w \pi r_g^2 |v_{I\|}| v_{I\|} \cos(\alpha) \tag{50}$$

$$Q_\xi^{wa} = \sum_{i=1}^{n_{dg}} Q_{i\xi}^{wa} \tag{51}$$

$$Q_\eta^{wa} = \sum_{i=1}^{n_{dg}} Q_{i\eta}^{wa} \tag{52}$$

$$
\begin{aligned}
Q_\alpha^h = & \sum_{i=1}^{n_{dg}} Q_{i\xi}^h (h_{ipg} - d_{S\text{bott}}) \cos(\alpha) \\
& + \sum_{i=1}^{n_{dg}} Q_{i\eta}^h (h_{ipg} - d_{S\text{bott}}) \sin(\alpha) \qquad (53)
\end{aligned}
$$

$$
\begin{aligned}
Q_\alpha^{wa} = & \sum_{i=1}^{n_{dg}} Q_{i\xi}^{wa} (h_{ipg} - d_{S\text{bott}}) \cos(\alpha) \\
& + \sum_{i=1}^{n_{dg}} Q_{i\eta}^{wa} (h_{ipg} - d_{S\text{bott}}) \sin(\alpha) \qquad (54)
\end{aligned}
$$

In (49) and (50), the last term represents the drag force on the flat surface at the bottom of the floater. It is approximately computed from the velocities of the first discretized cylinder and using the formula for the drag of a flat plate perpendicular to the flow (C_{dgb} is the drag coefficient for this case). It is supposed to be applied on the center of the first cylinder. In (53) and (54), $(h_{ipg} - d_{S\text{bott}})$ is the distance between BS and the point where the forces are applied. No momentum is generated by the drag force acting on the bottom surface of the floater, because it is placed on the axis of the floating structure.

Model Derivation: Summing up, the overall forces that appear in (7) are given by $Q_\xi = Q_\xi^{we} + Q_\xi^b + Q_\xi^t + Q_\xi^{wi} + Q_\xi^{wa} + Q_\xi^h$, $Q_\eta = Q_\eta^{we} + Q_\eta^b + Q_\eta^t + Q_\eta^{wi} + Q_\eta^{wa} + Q_\eta^h$, and $Q_\alpha = Q_\alpha^{we} + Q_\alpha^b + Q_\alpha^t + Q_\alpha^{wi} + Q_\alpha^{wa} + Q_\alpha^h$. Finally, the system (7) is obtained by applying the Lagrange equation to the total kinetic energy of the system, given by $E_k = (1/2)(M_S + m_x)v_\xi^2 + (1/2)(M_S + m_y)v_\eta^2 + (1/2)M_N v_N^2 + (1/2)M_P v_P^2 + (1/2)(J_S + J_N + J_P)\omega^2$. Here, J_S, J_N, and J_P are the moments of inertia of systems S, N, and P, m_y is the added mass of the floating structure in direction parallel to its axes and v_N and v_P are the velocities of BN and BP, i.e., $v_N = \sqrt{(v_\xi + d_N\omega\cos\alpha)^2 + (v_\eta + d_N\omega\sin\alpha)^2}$ and $v_P = \sqrt{(v_\xi + d_P\omega\cos\alpha)^2 + (v_\eta + d_P\omega\sin\alpha)^2}$. System (7) is derived by computing all the derivatives and setting $M_X = M_S + m_x + M_N + M_P$, $M_Y = M_S + m_y + M_N + M_P$, $M_d = M_N d_N + M_P d_P$, and $J_{TOT} = J_S + J_N + J_P + M_N d_N^2 + M_P d_P^2$.

APPENDIX II

Tables V–VII shows main parameters of the offshore wind turbine (1), (2), and states and inputs of the offshore wind turbine model.

ACKNOWLEDGMENT

The authors would like to thank L. Serri, E. Lembo, C. Casale, and C. Sandroni for their fruitful discussions.

REFERENCES

[1] J. M. Jonkman and D. Matha, "Dynamics of offshore floating wind turbines: Analysis of three concepts," *Wind Energy*, vol. 14, no. 4, pp. 557–569, May 2011.

[2] Executive committee of the implementing agreement for co-operation in the research, development, and deployment of wind energy systems of the international energy agency PWT Communications, "2010 IEA wind annual report," LLC, Boulder, CO, USA, Annu. Rep., 2011.

[3] L. Y. Pao and K. E. Johnson, "A tutorial on the dynamics and control of wind turbines and wind farms," in *Proc. Amer. Control Conf.*, 2009, pp. 2076–2089,

[4] G. Botta, C. Casale, E. Lembo, L. Serri, and S. Viani, "Resource and technology assessment for evaluating Italy's offshore wind energy potential," in *Proc. Int. Conf. Clean Electr. Power*, Jun. 2009, pp. 507–513.

[5] J. Jonkman and D. Matha, "A quantitative comparison of the responses of three floating platforms," Nat. Renew. Energy Lab., Golden, CO, USA, Tech. Rep. NREL/CP-46726, 2010.

[6] C. Casale, E. Lembo, L. Serri, and S. Viani, "Preliminary design of a floating wind turbine support structure and relevant system cost assessment," *Wind Eng.*, vol. 34, no. 1, pp. 29–50, May 2010.

[7] J. M. Jonkman and P. D. Sclavounos, "Development of fully coupled aeroelastic and hydrodynamic models for off-shore wind turbines," in *Proc. AIAA/ASME Wind Energy Symp.*, Jan. 2006, pp. 1–21.

[8] H. Namik, K. Stol, and J. Jonkman, "State-space control of tower motion for deepwater floating off-shore wind turbines," in *Proc. AIAA/ASME Wind Energy Symp.*, Jan. 2008, pp. 1–18.

[9] J. M. Jonkman, "Influence of control on the pitch damping of a floating wind turbine," in *Proc. ASME Wind Energy Symp.*, 2008, pp. 1–20.

[10] T. J. Larsen and T. H. Hanson, "A method to avoid negative damped low frequent tower vibrations for a floating, pitch controlled wind turbine," *J. Phys., Conf. Ser.*, vol. 75, no. 1, p. 012073, 2007.

[11] J. Jonkman, "Dynamics modeling and loads analysis of an offshore floating wind turbine," M.S. thesis, Dept. Aerosp. Eng. Sci., Colorado Univ., Golden, CO, USA, 2007.

[12] J. M. Jonkman, "Dynamics of offshore floating wind turbines: Model development and verification," *Wind Energy*, vol. 12, no. 5, pp. 459–492, 2009.

[13] J. Jonkman, S. Butterfield, W. Musial, and G. Scott, "Definition of a 5-Mw reference wind turbine for offshore system development," *Nat. Renew.* Energy Lab., Golden, CO, USA, Tech. Rep. NREL/TP-500-38060, 2009.

[14] A. R. Henderson and M. H. Patel, "On the modelling of a floating offshore wind turbine," *Wind Energy*, vol. 6, no. 1, pp. 53–86, 2003.

[15] D. Matha, T. Fischer, and M. Kuhn, "Model development and loads analysis of a wind turbine on a floating offshore tension leg platform," Nat. Renew. Energy Lab., Golden, CO, USA, Tech. Rep. NREL/CP-500-46725, 2010.

[16] M. Strobel, F. Vorpahl, C. Hillmann, X. Gu, A. Zuga, and U. Wihlfahrt, "The onwind modelica library for offshore wind turbines-implementation and first results," in *Proc. 20th Int. Offshore Polar Eng. Conf. IWES*, 2010, pp. 1–7.

[17] A. Cordle and J. Jonkman, "State of the art in floating wind turbine tools," in *Proc. 21st Int. Offshore Polar Eng. Conf.*, 2011, pp. 367–375.

[18] J. Doyle, B. Francis, and A. Tannenbaum, *Feedback Control Theory*. New York, USA: Macmillan, 1990.

[19] S. Skogestad and I. Postlethwaite, *Multivariable Feedback Control, Analysis and Design*. New York, USA: Wiley, 2005.

[20] E. A. Bossanyi, "Wind turbine control for load reduction," *Wind Energy*, vol. 6, no. 3, pp. 229–244, 2003.

[21] I. Munteanu, N. A. Cutululis, A. I. Bratcu, and E. Ceangă, "Optimization of variable speed wind power systems based on a lqg approach," *Control Eng. Pract.*, vol. 13, no. 7, p. 903–912, Jul. 2005.

[22] F. D. Bianchi, R. J. Mantz, and C. F. Christiansen, "Gain scheduling control of variable-speed wind energy conversion systems using quasi-LPV models," *Control Eng. Pract.*, vol. 13, no. 2, p. 247–255, 2005.

[23] B. Boukhezzar and H. Siguerdidjane, "Nonlinear control of variable speed wind turbines without wind speed measurement," in *Proc. 44th IEEE Conf. Decision Control*, Dec. 2005, pp. 3456–3461.

[24] B. Boukhezzar, L. Lupu, H. Siguerdidjane, and M. Hand, "Multivariable control strategy for variable speed, variable pitch wind turbines," *Renew. Energy*, vol. 32, no. 8, p. 1273–1287, 2007.

[25] B. Boukhezzar and H. Siguerdidjane, "Comparison between linear and nonlinear control strategies for variable speed wind turbines," *Control Eng. Pract.*, vol. 18, no. 12, p. 1357–1368, Dec. 2010.

[26] K. E. Johnson, L. Y. Pao, M. J. Balas, and L. J. Fingersh, "Control of variable-speed wind turbines," *Control Syst. Mag.*, vol. 26, no. 3, pp. 70–81, 2006.

[27] C. Wang and G. Weiss, "Self-scheduled LPV control of a wind driven doubly-fed induction generator," in *Proc. 45th IEEE Conf. Decision Control*, Dec. 2006, pp. 1246–1251.

[28] C. Wang and G. Weiss, "Integral input-to-state stability of the drive train of a wind turbine," in *Proc. 46th IEEE Conf. Decision Control*, Dec. 2007, pp. 6100–6105.

[29] I. Munteanu, A. I. Bratcu, N. A. Cutululis, and E. Ceangă, *Optimal Control of Wind Energy Systems, Towards a Global Approach*. New York, USA: Springer-Verlag, 2008.

[30] E. Bossanyi, B. Savini, M. Iribas, M. Hau, B. Fischer, D. Schlipf, T. van Engelen, M. Rossetti, and C. E. Carcangiu, "Advanced controller research for multi-MW wind turbines in the UPWIND project," *Wind Energy*, vol. 15, no. 1, pp. 119–145, Jan. 2012.

[31] H. Namik and K. Stol, "Individual blade pitch control of floating offshore wind turbines," *Wind Energy*, vol. 13, no. 1, pp. 74–85, 2009.

[32] F. Nielsen, T. Hanson, and B. Skaare, *Integrated Dynamic Analysis of Floating Offshore Wind Turbines*. New York, USA: ASME, 2006.

[33] B. Connor, S. Iyer, W. Leithead, and M. Grimble, "Control of a horizontal axis wind turbine using H infinity control," in *Proc. 1st IEEE Conf. Control Appl.*, vol. 1. Sep. 1992, pp. 117–122.

[34] M. Grimble, "Horizontal axis wind turbine control: Comparison of classical, LQG and H_∞ designs," *Dynamics Control*, vol. 6, no. 2, pp. 143–161, 1996.

[35] M. Lima, J. Silvino, and P. de Resende, "H_∞ control for a variable-speed adjustable-pitch wind energy conversion system," in *Proc. IEEE Int. Symp. Ind. Electron.*, vol. 2. Jul. 1999, pp. 556–561.

[36] C. Nichita, D. Luca, B. Dakyo, and E. Ceangă, "Large band simulation of the wind speed for real time wind turbine simulators," *IEEE Trans. Energy Convers.*, vol. 17, no. 4, pp. 523–529, Dec. 2002.

[37] F. Bianchi, H. De Battista, and R. Mantz, *Wind Turbine Control Systems: Principles, Modelling and Gain-Scheduling Design* (Advances in Industrial Control), A. Lavoisier Ed. New York, USA: Springer-Verlag, Jul. 2006.

[38] S. Chakrabarti, *Handbook of Offshore Engineering*. New York, USA: Elsevier, 2005.

[39] N. Kelley, "Full vector (3-D) inflow simulation in natural and wind farm environments using an expanded version of the SNLWIND (Veers) turbulence code," Nat. Renew. Energy Lab., Golden, CO, USA, Tech. Rep. NREL/TP-442-5225, 1992.

[40] L. Holthuijsen, *Waves in Oceanic and Coastal Waters*. Cambridge, U.K.: Cambridge Univ. Press, 2007.

[41] P. Spanos and S. Bhattacharjee, "Stochastic characterization of ocean depth and filter approximations for wave kinematics," *Appl. Ocean Res.*, vol. 16, no. 3, pp. 177–184, 1994.

[42] S. Massel, *Ocean Surface Waves: Their Physics and Prediction*. Singapore: World Scientific, 1996.

[43] T. Burton, D. Sharpe, N. Jenkins, and E. Bossanyi, *Wind Energy*. New York, USA: Wiley, 2001.

[44] R. Salas-Cabrera, J. C. Mayo-Maldonado, J. De León-Morales, J. C. Rosas-Caro, E. Salas-Cabrera, R. Castillo-Ibarra, R. Castillo-Gutierrez, M. Gomez-Garcia, H. Cisneros-Villegas, A. Gonzalez-Rodriguez, and C. Garcia-Guendulain, "On the adaptive estimation of the wind speed for a wind turbine," in *Proc. Eur. Wind Energy Conf. Exhibit.*, Jun. 2010, pp. 89–94.

[45] P. Odgaard, C. Damgaard, and R. Nielsen, "On-line estimation of wind turbine power coefficients using unknown input observers," in *Proc. 17th World Congr. Int. Federat. Autom. Control*, Jul. 2008, pp. 10646–10651.

[46] H. Li, K. Shi, and P. McLaren, "Neural-network-based sensorless maximum wind energy capture with compensated power coefficient," *IEEE Trans. Ind. Appl.*, vol. 41, no. 6, pp. 1548–1556, Nov.–Dec. 2005.

[47] J. Manwell, J. McGowan, and A. Rogers, *Wind Energy Explained*. New York, USA: Wiley, 2002.

[48] M. Hansen, A. Hansen, T. Larsen, S. Øye, P. Sørensen, and P. Fuglsang, "Control design for a pitch-regulated, variable speed wind turbine," Riso Nat. Lab., Roskilde, Denmark, Tech. Rep. RISO-R-1500, 2005.

[49] B. Munson, D. Young, T. Okiishi, and W. Huebsch, *Fundamentals of Fluid Mechanics*, 6th ed. New York, USA: Wiley, 2009.

[50] T. Glad and L. Ljung, *Control Theory: Multivariable and Nonlinear Methods*. Boca Raton, FL, USA: CRC Press, 2000.

[51] H. Bindner and F. Risø, "Active control: Wind turbine model," Risø Nat. Lab., Roskilde, Denmark, Tech. Rep. Risø-R-920(EN), 1999.

[52] B. M. Sumer and J. Fredsøe, *Hydrodynamics Around Cylindrical Structures* (Advanced Series on Ocean Engineering), 26th ed. Singapore: World Scientific, 2006.